Cryo-electron tomography reveals how COPII assembles on cargo-containing membranes

Euan Pyle[1,3], Giulia Zanetti*[1,2,3]

[1.] *Institute of Structural and Molecular Biology, Birkbeck College, London, UK*

[2.] *Institute of Structural and Molecular Biology, UCL, London, UK*

[3.] *The Francis Crick Institute, London, UK*

**Correspondence: giulia.zanetti@crick.ac.uk, g.zanetti@bbk.ac.uk, g.zanetti@ucl.ac.uk*

Abstract

Proteins traverse the eukaryotic secretory pathway via membrane trafficking between organelles. The COPII coat mediates the anterograde transport of newly synthesised proteins from the endoplasmic reticulum, engaging cargoes with wide ranges of sizes and biophysical properties. The native architecture of the COPII coat and the cargo-dependent regulation of its assembly remain poorly understood. Here, we have reconstituted COPII-coated membrane carriers using purified *S. cerevisiae* proteins and cell-derived microsomes as a native membrane source. Using cryo-electron tomography with subtomogram averaging, we demonstrate that the COPII coat binds cargo and forms largely spherical vesicles from native membranes. We reveal the architecture of the inner and outer coat layers and shed light on how spherical carriers are formed. Our results provide novel insights into the architecture and regulation of the COPII coat and challenge our current understanding of how membrane curvature is generated.

Introduction

Eukaryotic cells utilise the secretory pathway to transport proteins and lipids to their required locations within the cell. Approximately one in three proteins are translocated in the endoplasmic reticulum (ER) upon synthesis and are trafficked to the Golgi apparatus as the first step of the secretory pathway[1]. Anterograde transport of proteins from the ER to the Golgi is facilitated by coat protein complex II (COPII)-coated membrane carriers. The COPII coat assembles on the cytosolic side of the ER membrane, generating membrane curvature to form coated carriers, while specifically recruiting and enveloping newly-synthesised cargo proteins[2,3].

COPII comprises of 5 proteins (Sar1, Sec23, Sec24, Sec13 and Sec31) which are essential and highly conserved from yeast to humans[3]. COPII assembly is initiated by the small GTPase Sar1, which inserts its N-terminal amphipathic helix into the outer leaflet of the ER upon nucleotide exchange, an event catalysed by the ER-resident GTP Exchange Factor (GEF) Sec12[4,5]. Membrane-bound Sar1 recruits heterodimeric Sec23/24 to form the inner layer of the COPII coat, with Sec24 acting as the main cargo-binding subunit[6,7]. The outer coat layer is formed when heterotetrametric rod-shaped Sec13-31 complexes are recruited to budding sites, via interaction of Sec31 with Sec23/Sar1, and assemble in a cage-like arrangement[8–10]. Polyhedral cages assemble *in vitro* when purified Sec13-Sec31 heterotetramers are incubated in the absence of any membrane[10,11]. The detachment of Sar1 from the membrane is triggered by GTP hydrolysis, stimulated by its cognate GTP-ase Activating Protein (GAP) Sec23, and further accelerated by binding of Sec31[12]. Sar1 GTP hydrolysis is thought to destabilise the coat; however, the dynamics and regulation of coat disassembly are poorly understood.

Previously, we set out to determine the structure of the *S. cerevisiae* COPII coat reconstituted *in vitro* from giant unilamellar vesicles (GUVs) using cryo-electron tomography (cryo-ET) with subtomogram averaging (STA)[13–16]. We showed that COPII forms coated tubes on GUVs and that the inner and outer coat layers both arrange into pseudo-helical lattices that wrap around the tubular membrane. High-resolution STA yielded atomic models describing coat interactions and allowed us to design coat mutants where assembly interfaces are disrupted[15]. We found that the two interfaces that form the outer coat cage, formed by the N- and C-terminal domains of Sec31, are dispensable for membrane budding *in vitro* and in yeast cells lacking the GPI-anchored protein cargo adaptor Emp24[15,17]. Moreover, when the interface between inner coat lattice subunits was weakened by mutation, budded membranes switch from a tubular to a spherical profile, indicating that membrane curvature is generated by a complex network of interactions spanning both coat layers[15].

COPII-coated membrane carriers are known to adopt a range of sizes and shapes, which may be important to adapt to the wide range of cargoes that need to be accommodated. However, it remains unclear how coat assembly is regulated to achieve a variety of membrane carrier sizes[3,18,19]. Whilst our previous studies found that purified *S. cerevisiae*

COPII forms extended tubules on GUVs, electron microscopy studies of cell sections suggest that membrane carriers *in vivo* are spherical vesicles 50-100 nm wide[20–22], raising the question of which components of native membrane composition affect coat assembly and budding morphology. It also remains unclear how the tightly packed inner coat assembly is compatible with cargo binding by the Sec24 subunits. To answer these questions, we carried out *in vitro* reconstitution of COPII budding using native ER membrane sources directly derived from yeast, referred to as microsomes. In striking comparison to the tubules COPII forms on GUVs, cryo-ET revealed that the majority of coated membranes are pseudo-spherical. We used STA[16,23,24] to obtain the structures of the inner and outer coat assembled on native membranes. We found that the inner coat layer assembles similarly to its tubular arrangement, but forms limited patches of coat that are randomly oriented around a spherical membrane. Cargo density could be detected within the inner coat array, in the space between inner coat subunits, indicating that lateral assembly of Sar1-Sec23-24 heterotrimers can occur while small or flexible cytosolic domains of cargo molecules are accommodated in between. Finally, subtomogram analysis of the outer coat layer revealed multiple points of flexibility which were not previously described, increasing the complexity of the outer coat network, and challenging the current model that the assembly of the outer coat into a polyhedral cage is the main driver of membrane curvature.

Results

COPII Forms Coated Pseudo-Spherical Vesicles on Microsomes

In order to reconstitute COPII budding *in vitro* from native membrane sources, we incubated purified *S. cerevisiae* COPII proteins with *S. cerevisiae* ER-enriched microsomes and a non-hydrolysable GTP analogue (GMP-PNP) (Figure 1A and Supplementary Figure 1A). Imaging these budding reactions using cryo-ET revealed that COPII primarily forms vesicles (96.3 % of all coated membranes) on microsomal membranes which are clearly coated with both the inner and outer coat (Figure 1B). Only a minority of coated tubules were observed (3.7%), in striking comparison to previous reconstitutions using GUVs (91.4% tubules) (EMPIAR-11257).

The microsome-derived COPII coated vesicles are significantly smaller than the donor membranes, measured in a control sample where GDP was supplemented in place of GMP-PNP, demonstrating that the membrane is being actively deformed by COPII (Figure 1C). Most vesicles were complete and not attached to other membranes, with only a handful of instances where coated vesicles were connected to other membranes via a constricted neck (Figure 1B and Supplementary Figure 1B-F). Given that we used non-hydrolysable GTP analogues and performed no centrifugation or other mechanical perturbation of the sample, this suggests that vesicle scission from donor membranes does not depend on GTP hydrolysis.

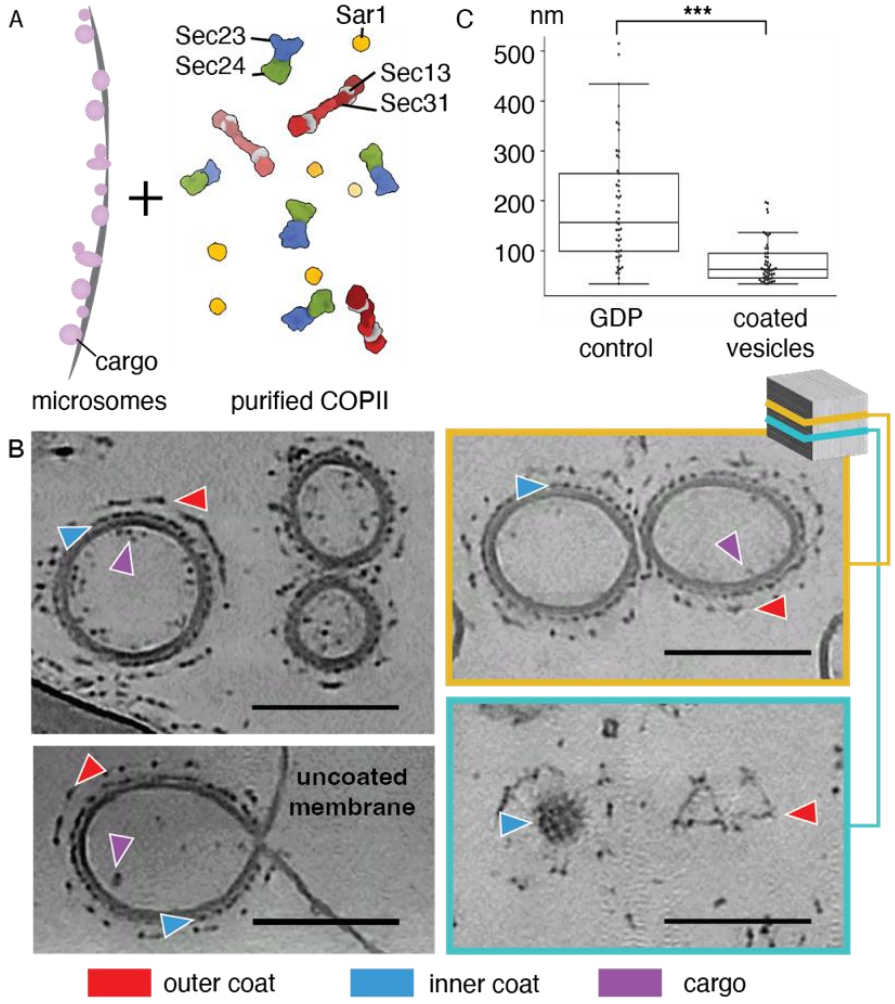

Figure 1 *(A) Schematic of the in vitro reconstitution approach. (B) XY slices of representative reconstructed tomograms where instances of inner coat, outer coat and cargo are labelled with blue, red and purple arrowheads respectively. In the bottom left panel an example of a vesicle connected to its origin membrane via a neck is shown. The right panels represent two Z slices of the same tomogram. The bottom slice shows both the inner and outer coat layers of neighbouring vesicles. Scale bar = 100 nm (C) Membrane diameters were measured from a control reconstitution reaction where GDP was used and compared with the diameters of coated membranes obtained in the presence of GMP-PNP.*

The COPII Inner Coat Lattice Assembles in Small Patches on Vesicles

Previous high-resolution STA structures of GUV-derived tubules showed that the inner coat assembles laterally to form a pseudo-helical lattice[15,16]. To assess if and how the previously characterised assembly interfaces can give rise to spherical vesicles, we used STA to obtain a structure of the inner coat on vesicles (Figure 2A and 2B). We found that the arrangement of the inner coat is analogous to that previously described on tubes, with Sar1-Sec23-Sec24 trimers assembling laterally and longitudinally in an ordered lattice (Figure 2A-C). At the resolution obtained (14.5 Å), there were no noticeable differences in the overall structure of the inner coat between the vesicles and the tubes, aside from the underlying membrane

having spherical rather than tubular curvature. Consequently, we could unambiguously fit a previous high-resolution structure (PDB: 8BSH) of the inner coat into the density. However, the overall arrangement of the inner coat lattice differs significantly. On spherical vesicles, the inner coat lattice forms in small patches (Figure 2C). These patches can be orientated in different directions to one another on the same vesicle, suggesting that separate inner coat arrays can co-exist at multiple sites on the vesicle surface (Figure 2C).

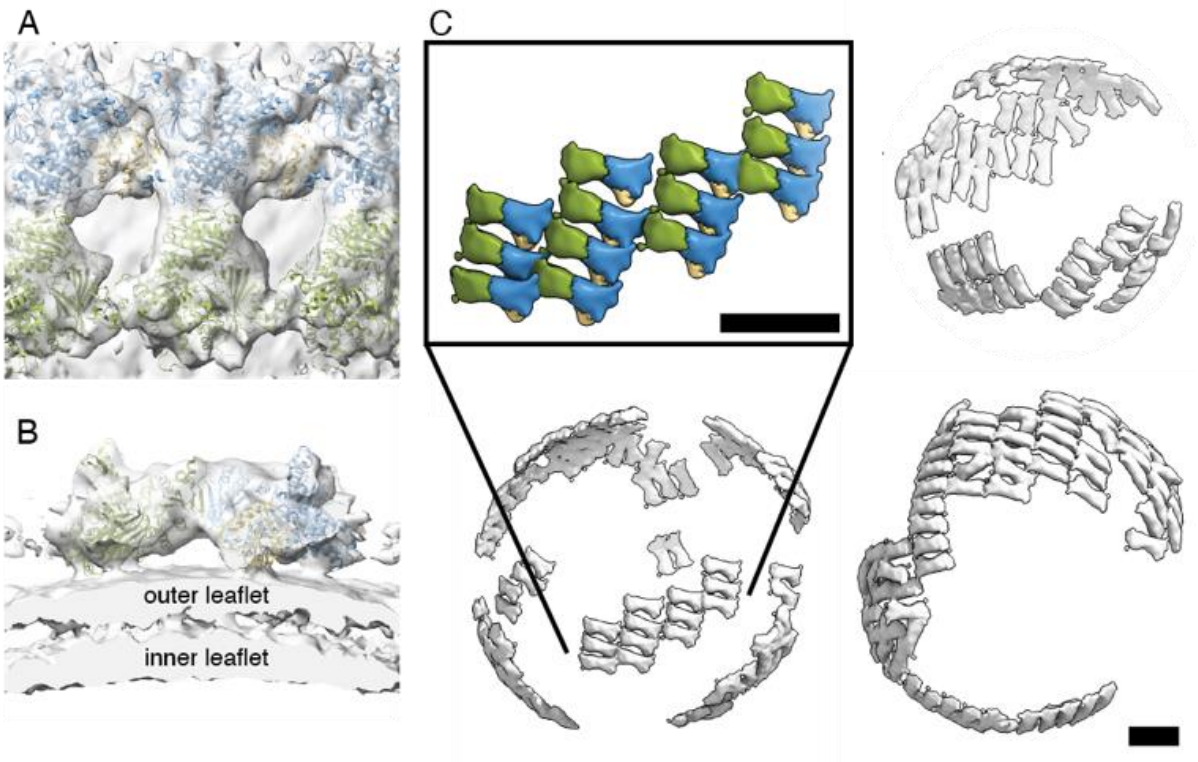

Figure 2 *(A and B) Subtomogram average of inner coat on vesicles fitted with three copies of the Sec23-Sec24-Sar1 heterotrimer atomic model (PDB: 8BSH) with Sar1 in yellow, Sec23 in blue, and Sec24 in green. View in (A) is looking down towards the membrane (top view), while (B) cuts through the membrane (side view). (C) A low-pass filtered STA structure is mapped back in space. Three examples are shown to demonstrate the small patches arrangement of the lattice. Inset: a close up of one of the patches with the same colour code as in (A). Scale bar= 10 nm.*

Cargo Binds Within the COPII Inner Coat Lattice

We next set out to establish whether inner coat lattice formation is compatible with the presence of cargo. The inner coat is known to bind to a range of cargo molecules on several previously characterised binding sites on Sec24, including: the A-site located on the Sec24 side distal to Sar1 within the heterotrimer, and the B-, C- and D-sites located closely to one other on the opposite face of Sec24[25,26]. If cargo is bound to Sec24 in our structure, we would expect to see extra protein density proximal to the known binding sites. As we were unable to visualise density clearly above noise levels, we calculated the difference map between our STA structure of the inner coat on microsomes and a map generated by low-pass filtering the fitted model of the Sec23-Sec24-Sar1 heterotrimer to 14.5 Å. From the difference map, we found strong signal in the space between neighbouring Sec24 subunits, indicative of the presence of protein density and thus, potentially cargo (Figure 3A). The

difference density seems located close to the B-, C-, and D- cargo binding sites of Sec24. As a control, we repeated the same experiment using the previously determined structure of the inner coat on cargo-less GUVs[16], for which the difference map appears clear of any density (Figure 3B).

Due to the presence of a wide range of structurally diverse cargoes on the microsomal membranes, it was not possible to resolve the bound protein density to anything other than a shapeless 'blob' (Figure 3A). It is likely that the cargoes bound to the inner coat within the lattice are either small, flexible, or both, as cargoes with bulky cytosolic domains would be sterically prevented from binding in the 50Å-wide space between neighbouring heterotrimers (Figure 3A). Whilst we expect different subsets of Sec24 molecules to be bound to cargos of different sizes, or not at all, we were unable to reproducibly differentiate between them using 3D classification. This is likely due to the high amount of compositional and conformational heterogeneity of the cargo molecules.

To further test whether the inner coat lattice formation is compatible with cargo binding, we reconstituted COPII budding using GUVs whose surface was enriched with the cytosolic domain of a small cargo protein, Sed5 from *S. cerevisiae*. Sed5 contains two known Sec24 binding motifs specific for the A- and B-sites (YNNSNPF and LMLME, respectively)[25]. AlphaFold predictions of Sed5 structure (PDB ID: AF-Q01590-F1) suggest that these are both found in a highly flexible region characterised by very low confidence scores, allowing Sed5 to bind in the small space between inner coat units (Supplementary Figure 2A).

First, we purified the Sed5 cytosolic domain (residues 1 to 319) to high purity and homogeneity (Supplementary Figure 2B). We enriched the surface of the GUVs with Sed5 by the association of Ni-NTA tagged lipids in the GUVs to a C-terminal His_6 tag in the purified Sed5, cloned in place of the transmembrane domain (Figure 3C, inset). We verified the successful association of Sed5 to the membrane by liposome flotation assays (Supplementary Figure 2B). We then carried out COPII budding reconstitution *in vitro* using Sed5-enriched GUVs (Figure 3C). Imaging these budding reactions using cryo-electron tomography revealed that COPII primarily forms tubes (88.8 % of all coated membranes) (Figure 3D), similarly to previous studies with cargo-less GUVs[15]. The inner and outer coat lattices were clearly visible on these tubes (Figure 3D).

To establish whether Sed5 was bound within the inner coat lattice, we carried out STA to generate a high-resolution (4.1 Å) structure of the inner coat lattice (Supplementary Figure 3A-C). The Sed5-bound map was essentially identical to previous structures lacking cargo, but crucially, we saw unambiguous protein density in one of the known Sed5 binding pockets in correspondence to the B-site (Figure 3E and F). We were unable to resolve any further Sed5 protein density outside of the known binding pocket on Sec24. This is unsurprising given that the Sec24 binding motifs on Sed5 were predicted to be in a highly flexible and disordered region (Supplementary Figure 2A). Nevertheless, we have confirmed that Sed5, as presumably other small and flexible cargo proteins, can bind to the inner coat without disrupting the lattice.

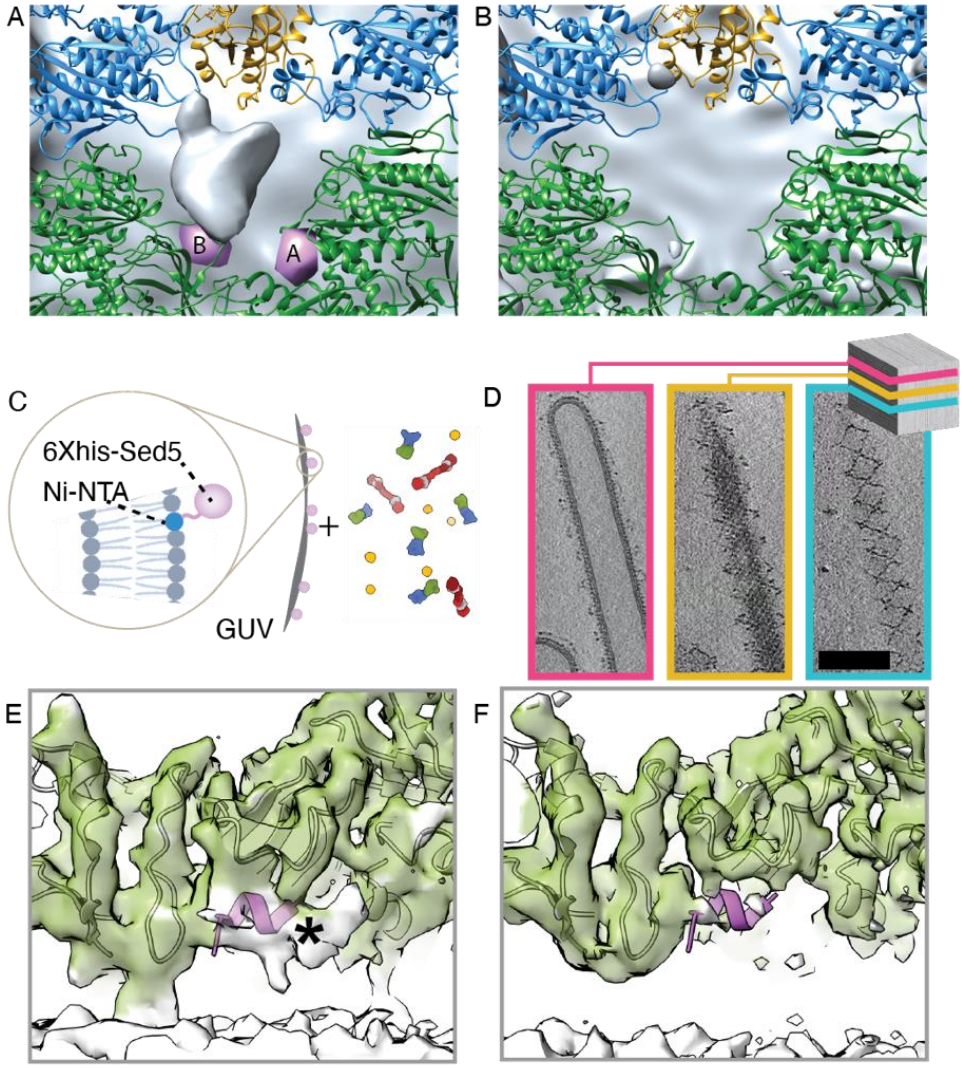

Figure 3 *(A) Difference map between the subtomogram average of the inner coat on microsomes and a 14 Å low-pass filtered volume representation of the fitted model of the inner coat from cargo-less GUVs (PDB: 8BSH) with Sar1 in yellow, Sec23 in blue, and Sec24 in green. The Sec24 A- and B- cargo-binding sites are represented with pink blobs generated from bound cargo peptides described in previous X-ray crystallography studies (PDB: 1PD0, 1PCX). (B) as in (A) but using the STA map previously obtained from GUVs (EMD-15949), and low-pass filtered to 14 Å. (C) Schematic of the in vitro reconstitution of COPII budding from Sed5-enriched GUVs, the inset highlights details of His_6-tagged Sed5 associating to the Ni-NTA tagged lipids on the GUVs. (D) XY slices through a representative tomogram of Sed5-enriched GUV budding reactions at different Z heights displaying the coated tube morphology (pink, z=162), and the inner (yellow, z=137) and outer (blue, z=128) coat arrangements. Scale bar = 100 nm. (E) Detail of the STA map of Sed5-bound inner coat showing the region around the Sec24 B-site. Density closer than 3.5 Å to the fitted model of the inner coat (PDB: 8BSH) is shown in green whilst white density corresponds to regions of the map that are not explained by the fitted model. The model of a Sec24-bound peptide from Bet1 cargo (PDB: 1PCX), which contains the same B-site binding motif as Sed5 (LxxLE), is also fitted to highlight the location of the B-site and is shown in purple. White density in correspondence of this peptide is marked with an asterisk. (F) As in (E) but displaying the map obtained from cargo-less GUV reconstitution (EMDB-15949).*

The COPII Outer Coat is Structurally and Morphologically Heterogeneous on Vesicles

The Sec13-Sec31 outer coat layer was clearly visible on microsome-derived COPII-coated vesicles (Figure 1B). Manual inspection of denoised tomograms revealed that the outer coat was generally arranged in cage-like structures, with “rods” of Sec13-31 acting as edge elements (Figure 4A). Multiple arrangements of these Sec13-31 rods were observed. In many instances, four rods converge to form vertices through the interaction of Sec31 N-terminal beta-propeller domains, in the canonical manner previously described in *in vitro* assembled protein-only cages, and reconstituted tubules[10,11,15] (Figure 4A, blue lozenges). We also observed rods where one or both of the Sec31 N-terminal domains bind to the Sec31 dimerisation domain (Figure 4A, orange ‘Ts’). We previously described a similar interaction on tubules, and proposed that it stabilises the outer coat when neighbouring patches are ‘out of phase’ with respect to one another and vertices cannot form[15]. Finally, we observe an entirely novel interaction where 5 rods converge to form vertices (Figure 4A, pink pentagons). The variety of rod arrangements presented here suggests that the outer coat is highly morphologically heterogenous on vesicles, in stark contrast to the more regular outer coat morphology seen on tubes and on *in vitro* assembled membrane-less polyhedral cages.

The structures of the canonical outer coat vertex and Sec13-31 rods were resolved by STA to 11-12 Å for both the microsome-derived and the Sed5-enriched GUV samples. This resolution allowed unambiguous rigid-body fitting using previously determined atomic models (PDB: 2PM9 and 2PM6) (Figure 4B-C). For both vertices and rods, the Sed5-GUV and microsome-derived maps are very similar (Supplementary Figure 4). Previously, we showed that the Sec31 C-terminal domain binds to the dimerization domain of another Sec31 to form an ‘elbow’ (Figure 4C, black arrowheads) and hypothesized that this interaction is important to stabilise the coat. However, the microsome-derived structure contained a stronger and better-defined density for the C-terminal domain of Sec31 (Supplementary Figure 4E-F). Taken together, this suggests a more prominent role for this stabilising interaction in the context of the widely varying assembly seen on the spherical vesicles derived from microsomes compared to the GUV-derived tubules.

Analysis of the arrangement of the outer coat revealed further unexpected heterogeneity. By plotting the positions of the nearest vertex neighbours for all rods (Figure 4D), a general rhomboidal and triangular pattern emerged conveying the expected outer coat arrangement of rods with a vertex at each extremity (Figure 4D, dotted lines). However, the points representing the positions of the vertices relative to the centre of each rod did not form a sharp peak. Instead, the distribution of the distance of the vertices relative to the rods was very broad which suggested that the rods are not rigid. To investigate this further, we defined distinct classes of rods based their distance to their nearest vertex from within the ‘cloud’ of points (blue, purple, and red rings in Figure 4D). We reconstructed the corresponding classes of rods, generating three different maps which demonstrated

variation in rod structure (Figure 4E). Specifically, this analysis revealed high mobility around the two hinge regions located near the Sec13- and Sec31- β-propellers (Figure 4E, Supplementary Movie 1).

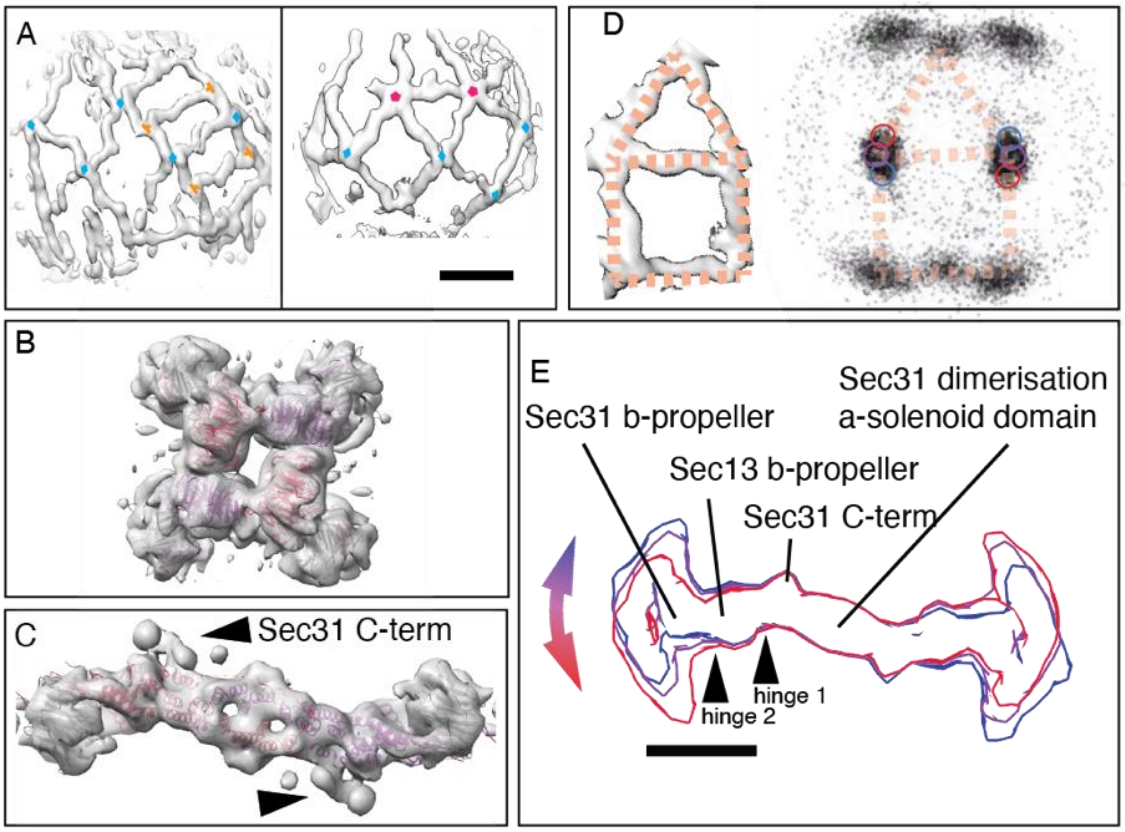

Figure 4 *(A) COPII outer coat arrangement on vesicles in denoised tomograms. Tomograms were masked to remove the inner coat for visual clarity. Blue lozenges indicate vertices with 4 rods converging, pink pentagons indicate vertices with 5 rods converging, and orange 'T's indicate non-vertex rod interactions. Scale bar = 30 nm. (B) STA map of the outer coat vertex on vesicles from microsomes at 11.4 Å, with four copies of the atomic model of the Sec13-Sec31 'vertex element' fitted (PDB: 2PM9) with Sec31 in red and purple, Sec13 in grey (C) STA map of the outer coat rod on vesicles at a resolution of 11.5 Å, with the atomic model of the Sec13-Sec31 'edge' element fitted (PDB: 2PM6). Colour code as in (B). (D) Left panel: an example density from a tomogram to show the typical arrangements of rods to form the edges of lozenges and triangles, highlighted by the superimposed dotted line in orange. Right panel: the position of vertices surrounding all rods is plotted: each black dot corresponds to the position of one vertex. The pattern appearing from clustering of nearest vertices corresponds to most rods being arranged in lozenges and triangles (orange dotted lines). (E) Variation of rod structures. Rods were selected according to the nearest vertices falling within regions defined by the red, purple and blue rings shown on (D) and were reconstructed as different classes. The resultant structures are overlayed and show movement around two major hinge regions. Scale bar = 10 nm.*

Discussion

We reconstituted COPII budding *in vitro* using *S. cerevisiae* microsomes as native membrane sources. Microsomes are cell-derived membranes which largely comprise of the ER.

Therefore, microsomes resemble the ER in their lipid composition, heterogeneity, and importantly, the presence of transmembrane and lumenal cargo proteins. In striking comparison to the COPII-coated tubules generated from GUVs, microsome-derived membrane carriers are mostly pseudo-spherical.

Subtomogram analysis of the coat on spherical vesicles showed that the inner coat Sar1-Sec23-24 heterotrimers assemble into small patches of lattice, in contrast to the continuous lattice found on tubules. The arrangements of neighbouring subunits in these small patches and in the extended lattice found on regular tubules are highly similar. Cargo protein density was detected within the inner coat lattice of microsome-derived vesicular carriers, indicating that small and/or flexible cargo cytosolic domains can be accommodated within the tightly packed inner coat. This was further confirmed by the reconstitution of the flexible Sed5 cytosolic domain onto GUVs, as COPII budding leads to formation of highly ordered tubules where a short Sed5 peptide can be detected bound to Sec24 B-site. Interestingly, we do not see any significant density for the Sed5 peptide bound to the A-site (Supplementary Figure 3D-E).

Subtomogram analysis of the coat assembled around spherical vesicles also revealed a highly variable and flexible outer coat cage consisting of Sec13-31 rods assembling with many different geometries. These geometries include rods converging with the Sec31 N-terminus to form canonical 4-way vertices, T-junctions with other rod's dimerization domain, as well as pentameric vertices. The rods themselves are highly flexible, with two major hinge points around the Sec13 β-propeller.

Overall, our findings that COPII morphology differs between microsomes and naked GUVs, in combination with our previous finding that the regions responsible for outer coat assembly are not necessary for budding[15], challenge the idea that the outer coat cage is the main driver of membrane curvature. We propose a new model for generation of membrane curvature by the COPII coat (Figure 5), where vesicle shape is mostly determined by inner coat assembly. According to this model, the extent of inner coat lattice formation drives membrane curvature. In the extreme case of undisturbed lattice assembly, as obtained *in vitro* where GTP hydrolysis is inhibited, no bulky proteins are present, and membrane sources are abundant, coated tubes are formed. In native conditions, where bulky proteins are present to disrupt inner coat lattice assembly, small patches of randomly oriented inner coat lattice will lead to formation of pseudo-spherical vesicles. In this scenario, the outer coat's ability to adapt to a continuous and varied range of growing curvature ensures effective binding and assembly of cages, which stabilise the coated vesicle. Of note, *in vitro* reconstitutions from GUVs using COPII mutants with weakened inner coat lattice interfaces also led to the formation of spherical profiles[15], supporting the proposed model.

The vast majority of vesicles we observed were detached from the donor membranes, with only a handful of instances of constricted necks. Here, we use a non-hydrolysable GTP analogue, and do not perform any centrifugation or mechanical perturbation aside from gentle pipetting to prepare our samples, suggesting GTP hydrolysis is not required for

scission. Interestingly, the coated spherical profiles we observed previously with COPII interface mutants on GUVs remained linked by constricted necks (like beads on a string)[15], suggesting that scission depends on factors present within the microsome membrane.

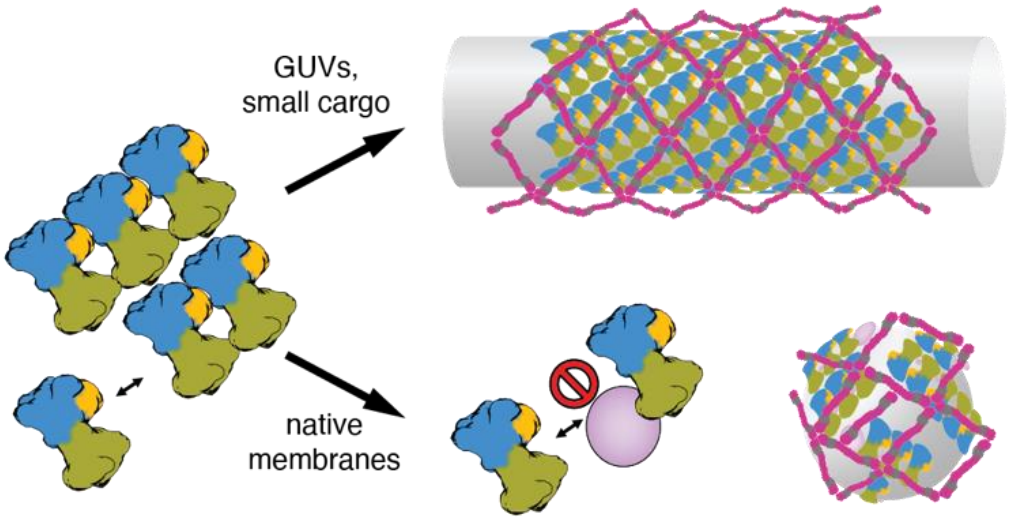

Figure 5*: Schematic describing the proposed model of COPII budding, where inner coat lattice assembly drives curvature of the membrane. If undisturbed, this leads to an extended pseudo-helical lattice and formation of coated tubes (top). In native conditions, where bulky protein (pink) are present, extensive assembly of inner coat is not possible and small patches randomly orient to generate near-spherical membranes.*

Materials and Methods

Cloning

Sed5 (UniProt: Q01590) (residues 1-319, truncating the transmembrane helix) was cloned from the *Saccharomyces cerevisiae* S288c genome into a pETM-11 expression vector linearised at the XhoI and XbaI restriction sites using In-Fusion (Takara) technology. A flexible triple-glycine linker was added between the C-terminal residue (319) of Sed5 and a His_6 tag. The primers are used were:

Fo: 5'- GGTGTCCTCCTCCTCTATTACTCTTTATCCTGTCGAAG -3'

Re: 5'- GAGGAGGAGGACACCACCACCACCACCAC -3'

Sec23/24, Sec13/31, and Sar1 constructs previously described in Hutchings *et al.* (2021)[15] were used here.

Protein Expression and Purification

The Sed5 pETM-11 vector was transformed into *Escherichia coli* (BL21) cells via heat shock. Cells were cultured at 37 °C with 220 rpm shaking in 2 L of LB media supplemented with kanamycin. When cultures reached an optical density between 0.7-1, 0.2mM IPTG was added, and the incubation temperature reduced to 16 °C. Culture pellets were harvested after approximately 16 hours by centrifugation and flash frozen in liquid nitrogen before storage at -80 °C.

Sed5 pellets from 2 L culture were thawed and resuspended in 20 mL Ni-A buffer (50 mM Tris (pH 8), 500 mM KCl, 0.1 % TWEEN 20 (v/v), 10 mM imidazole, 1 mM DTT) supplemented with 1 complete protease inhibitor tablet (Roche). 40 mg/mL lysozyme was added to the pellets, which were then stirred on ice for 20 minutes. Cells in the pellets were lysed using a cell disruptor. Unbroken cells were removed by ultracentrifugation at 20200 *xg* for 25 minutes. The supernatant was loaded onto a Ni-NTA 5 mL His-trap column (G.E. Biosciences) equilibrated with Ni-A buffer and washed with 5 column volumes of Ni-A buffer. Sed5 was eluted from the column via applying a linear gradient of Ni-B buffer (50 mM Tris (pH 8), 500 mM KCl, 0.1 % TWEEN 20 (v/v), 500 mM imidazole, 1 mM DTT). Fractions were analysed by SDS-PAGE and those containing Sed5 were pooled before 10x dilution in Q-A buffer (20mM Tris (pH 8.0), 0.1 % TWEEN-20 (v/v), 10 % glycerol (v/v), 1 mM DTT). Sed5 was loaded onto a 5 mL HiTrap Q column (G.E. Biosciences) equilibrated with Q-A buffer. The column was washed with 2 column volumes of Q-A buffer, and 2 column volumes of a mixture of 90 % Q-A buffer and 10 % Q-B buffer (20mM Tris (pH 8.0), 0.1 % TWEEN-20 (v/v), 10 % glycerol (v/v), 1 mM DTT, 1 M KCl). Sed5 was eluted with a linear gradient of Q-B buffer. Fractions were analysed by SDS-PAGE and those containing Sed5 were pooled and concentrated using a

protein concentrator with a 10 kDa molecular weight cut off to a final concentration of 0.5 mg/mL. Sed5 was separated into 100 μL aliquots and flash frozen.

The final step of Sed5 purification was carried out on the day of use. 1 aliquot of Sed5 was thawed before injection onto a Superdex 200 Increase 3.2/300 column equilibrated with HKM buffer (20 mM HEPES, 50 mM KOAc and 1.2 mM MgCl2, pH 6.8). Fractions containing Sed5 were identified by SDS-PAGE and pooled together.

The purified protein was confirmed as Sed5 by analysis with SDS-PAGE combined with gel sequencing by mass spectrometry at the Mass Spectrometry and Proteomics Facility at the University of St. Andrews.

Sec23/24, Sec13/31, and Sar1 were expressed and purified as described previously[15].

Liposome Flotation Assays

Liposomes were generated as previously described[27] using the 'Major-Minor' lipid mixture: 49 mol% phosphatidylcholine, 20 mol% phosphatidylethanolamine, 8 mol% phosphatidylerine, 5 mol% phosphatidic acid, 9 mol% phosphatidylinositol, 2.2 mol% phosphatidylinositol-4-phosphate, 0.8 mol% phosphatidylinositol-4,5-bisphosphate, 2 mol% cytidine-diphosphate-diacylglycerol, supplemented with 2 mol% TexasRed-phosphatidylethanolamine, 2 mol% Ni-NTA tagged lipids (18:1 DGS-NTA(Ni)), and 20% (w/w) ergosterol.

Liposomes were pre-mixed with the Sed5, and floatation assay experiments were performed without and with the addition of COPII components: 1 μM Sar1, 180 nM Sec23/24, 173 μM Sec13/31, 360 nM Sed5 with 1 mM GMP-PNP (Sigma-Aldrich), 2.5 mM EDTA (pH 8.0). All floatation assays contained 0.27 mM liposomes in a total volume of 75 μL. Liposome floatation reactions were mixed with 250 μL 1.2 M sucrose in HKM buffer in an ultracentrifuge tube. 320 μL 0.75 M sucrose in HKM was gently layered on top. A final layer of 20 μL HKM was then layered on top of the sucrose solutions. Ultracentrifuge tubes were loaded into a SW-55 Ti ultracentrifuge rotor before spinning at 280k *xg* at 4 °C for at least 16 hours. The top 20 μL of the sucrose gradient was carefully extracted before analysis via SDS-PAGE with silver staining.

Budding Reactions

Purified microsomes from *S. cerevisiae* were kindly provided by Liz Miller (MRC-LMB, Cambridge), prepared as described previously[28]. 1.5 mg of microsomes were washed three times carrying out the following steps: resuspending the microsomes in 1 mL B88 buffer (20 mM HEPES (pH 6.8), 150 mM KOAc, 250 mM sorbitol, 5 mM $Mg(OAc)_2$), pelleting membranes by centrifugation on a chilled benchtop centrifuge at 20,000 *xg* for 2 minutes, removing the supernatant, and resuspending the pellet in 50 μL B88 buffer. After washing, the pellets were diluted a further 8x, and chilled on ice before use in budding reactions.

Budding reactions in microsomes were prepared by incubating 1 μM Sar1, 180 nM Sec23/24, 173 μM Sec13/31 with 1 mM GMP-PNP (Sigma-Aldrich), 2.5 mM EDTA (pH 8.0) and 10 % microsomes (v/v).

GUVs were prepared by electroformation[29] from 10 mg/mL of a major-minor lipid mixture with 2 mol% Ni-NTA tagged lipids (described in the liposome floatation assay section) in a 2:1 chloroform:methanol solvent mixture, as described previously[14,30]. The lipid mixture was spread over two Indium Tin Oxide-coated glass slides. 300 mM sucrose was suspended in a silicon O-ring between these glass slides and GUVs were generated using a NanIon Vesicle Prep Pro. GUVs in the sucrose solution were added to 500 μL of 300 mM glucose and left to sediment overnight at 4 °C. The supernatant was discarded, leaving a 50 μL pellet of GUVs.

Budding reactions in GUVs with Sed5 were prepared by incubating 1 μM Sar1, 180 nM Sec23/24, 173 μM Sec13/31, 360 nM Sed5 with 1 mM GMP-PNP (Sigma-Aldrich), 2.5 mM EDTA (pH 8.0) and 10 % GUVs (v/v). GUVs were pre-mixed with the Sed5 prior to addition to the COPII components. Budding reactions were incubated for at least 30 minutes before vitrification for cryo-electron tomography.

Cryo-Electron Tomography Sample Preparation

5 nm BSA-blocked gold nanoparticles (BBI Solutions) were added to the budding reactions at a concentration of 10 % (v/v). 4 μL of budding reactions from GUVs or microsomes was added to glow-discharged Lacey Carbon Films on 300 Mesh Copper Grids (Agar Scientific), incubated for 60 seconds, before back-blotting on a Leica-GP2 plunge freezer in 95 % humidity and a 4 second blotting time. Vitrified grids were stored in liquid nitrogen prior to data collection.

Cryo-Electron Tomography Data Collection

Budding reactions with microsomes were imaged using cryo-electron tomography at the EMBL Imaging Center in Heidelberg on a Titan Krios microscope (Thermo Scientific) operated at 300 kV. The microscope was equipped with a SelectrisX energy filter (Thermo Scientific) and a Falcon 4 detector (Thermo Scientific) in counting mode. Pixel size was 1.526 Å and tilt series were taken with a defocus range of -3 μm to -5 μm. Tilt series were taken using a dose-symmetric tilt scheme[31] over a total exposure of 140 e^{-} $Å^{-2}$ with tilt angles ranging between -60 ° to +60 ° at a 3 ° increment. Data collection was controlled using SerialEM[32] and implementing PACE-tomo[33]. 765 high-quality tilt series were collected.

Budding reactions with GUVs and Sed5 were imaged using cryo-electron tomography at the EMBL Imaging Center in Heidelberg over two sessions of data collection on a Titan Krios microscope operated at 300 kV. The microscope was equipped with a K3 (Gatan) detector and energy filter. The first session was collected in super-resolution mode and the second session was collected in counting mode. Pixel size was 1.33 Å and tilt series were taken with a defocus range of -1.5 μm to -3.5 μm. Tilt series were taken using a dose-symmetric tilt

scheme[31] over a total exposure of 142 e^{-} $Å^{-2}$ with tilt angles ranging between -60 ° to +60 ° at a 3 ° increment. Data collection was controlled using SerialEM. 326 high-quality tilt series were collected.

Grids were screened and optimised at the ISMB EM Facility at Birkbeck College.

Cryo-Electron Tomography Data Processing

The microsomes dataset was processed using an Alpha-phase development version of RELION 5.0 (4.1-alpha-1-commit-d2053c) (manuscript in preparation). Initially, .mdoc files were renamed TS_[number]-style to ensure compatibility with RELION to Dynamo and vice versa scripts later in the processing workflow. Raw data then was imported into RELION 5.0. Individual tilt movies were motion corrected and averaged using whole frame alignment in the RELION implementation of MotionCor2[34,35]. CTF estimation was carried out using CTFFIND-4.1[36] with a defocus range of -25000 to -55000 Å and a maximum CTF resolution of 20 Å. Tilt series were manually inspected and poor tilt images were removed using a Napari plug-in (https://github.com/napari/napari/blob/main/CITATION.cff) provided as part of the Exclude tilt-images job-type in RELION 5.0. Tilt series were automatically aligned using the IMOD wrapper for fiducial-based alignment in RELION with a fiducial diameter of 8 nm. Tomograms were reconstructed in RELION at a pixel size of 12.208 Å for visual inspection and particle picking. Tomograms were denoised and missing wedge-corrected using IsoNet[37]. 8x binned CTF-corrected tomograms for use in PyTOM template matching[38] were manually generated using IMOD's *etomo*[39] function on the IMOD metadata generated by the Align tilt-series job-type in RELION.

The GUVs-Sed5 dataset was processed using the RELION4_Tomo_Robot (https://github.com/EuanPyle/relion4_tomo_robot/blob/master/CITATION.cff). Individual tilt movies were motion corrected and averaged using whole frame alignment with MotionCor2[34]. Movies collected in super resolution mode were binned by 2x during motion correction. Tilt series were created from individual tilt images using IMOD's *newstack* function. Tilt series were manually inspected using IMOD's *3dmod* visualisation function and bad tilts were removed using IMOD's *excludeviews* function. Tilt series were automatically aligned using Dynamo's automated fiducial-based alignment in the RELION4_Tomo_Robot's 'fast_mode' with a fiducial diameter of 5 nm[40]. CTF estimation was carried out using CTFFIND-4.1[36]. The dataset was then imported into RELION 4.0[16]. Tomograms were reconstructed in RELION at a pixel size of 10.64 Å for visual inspection and particle picking. Tomograms were denoised and missing wedge-corrected using IsoNet[37].

Subtomogram Averaging

Microsomes Dataset

Inner coat: The surface of vesicles in IsoNet-denoised tomograms was defined and segmented using the Pick Particle plug-in in Chimera as described previously[41,42]. The

coordinates of the vesicle surface were used to mask the tomograms to enable manual particle picking in UCSF Chimera which were assigned Euler angles normal to the membrane. Particles were extracted in 32 voxel boxes from IsoNet-denoised tomograms at a voxel size of 12.208 Å. Particles were assigned random in-plane rotation angles and were averaged to create a reference using Dynamo[40]. Particles were then aligned and averaged in Dynamo with the following conditions: a cone range of 10° was applied whilst 360° of in-plane rotation was allowed; particle translation was limited to 1 voxel in all directions due to the accuracy of the coordinates of the manually picked particles; a C2 symmetry was applied due to the pseudo-symmetry of the inner coat at low resolution; a mask covering the area of one inner coat subunit was applied; alignment was carried out for 100 iterations. The resulting Dynamo table was converted to a .star file using *dynamo2relion* (https://github.com/EuanPyle/dynamo2relion). Particles were imported into an Alpha-phase development version of RELION 5.0 (4.1-alpha-1-commit-d2053c) and extracted as pseudo-subtomograms at bin4 in 64 voxel boxes. A reference was reconstructed at the same box and voxel size using the Tomo Reconstruct Particle job-type. Particles were refined using Refine3D with the reference low-pass filtered to 30 Å, no mask applied, a particle diameter of 200 Å, and all Euler angles limited to local refinements of approximately 9 ° using the additional argument *--sigma_ang 3*. Poorly aligned particles were removed via 3D Classification without particle alignment, no mask applied, 6 classes, and a regularisation parameter (T value) of 0.2. A reference was reconstructed at bin1 in a box size of 196 voxels before the tilt series alignment for each tomogram was refined using Tomo Frame Alignment without fitting per-particle motion or deformations. Particles were re-extracted as pseudo-subtomograms at bin4 as before and refined as before using a mask over 1 inner coat subunit.

The structure generated by RELION was used to pick more particles in CTF-corrected tomograms with PyTOM template matching[38] with dose-weighting and CTF-correction applied.

Coordinates from PyTOM were imported into RELION 5.0. To remove junk particles, 3D classification was carried out with alignment using restricted Tilt and Psi Euler angles (*--sigma_rot 3 --sigma_psi 3*) but leaving in-plane rotation free, a mask over 1 inner coat unit and over part of neighbouring subunits, the map from the refined manually picked particle low-pass filtered to 25 Å as a reference, 4 classes, a T value of 0.1, and a particle diameter of 330 Å. Particles clearly resembling the COPII inner coat were kept, and refined under similar conditions to the preceding 3D classification. Particles were cleaned again using 3D classification without alignment with 6 classes and a T value of 0.2. The resulting particles.star file was merged with the manually picked particles generated earlier. Duplicate coordinates were deleted before. Particles were exported to a Dynamo table using *relion2dynamo* (https://github.com/EuanPyle/relion2dynamo) and were cleaned by Neighbour Analysis, as previously described[41]. Coordinates were converted back to a .star file using *dynamo2relion* and reimported into RELION. Particles were refined as before, but at bin2 and with all Euler angles limited to local refinements using *--sigma_ang 3.* One more

round of Tomo Frame Alignment, with per-particle motion, was carried out before Tomo CTF Refinement. A final refinement was carried out at bin2 with limited Euler angles using *--sigma_ang 1.5.*

A difference map, as described in Figure 3A, between this structure and the inner coat from cargo-less GUVs was generated as follows: a model of the inner coat from cargo-less GUVs (PDB: 8BSH) was fitted into the inner coat map from microsomes. A volume representation of the fitted model was generated using *molmap* in UCSF Chimera[43] at high resolution (2 Å) before low pass filtering to 14 Å in MATLAB. All maps were normalised to the same mean and standard deviation before the map from the fitted model was subtracted from our map from microsomes. Another difference map, as described in Figure 3B, was generated in the same way but using a 14 Å low pass filtered electron density map (EMDB-15949) corresponding to the fitted PDB model (PDB: 8BSH) instead of our map of the inner coat derived from microsomes.

Outer coat (vertex): Outer coat vertices were manually picked in 30 tomograms, as before for the inner coat particles. Particles were assigned Euler angles normal to their nearest membrane. Particles were extracted in 64 voxel boxes from RELION-reconstructed tomograms at a voxel size of 12.208 Å. Particles were averaged as before for the inner coat to form an initial average. Particles were then aligned and averaged in Dynamo as for the inner coat but with a translational shift of 4 voxels allowed and with a mask covering the vertex. The resulting map was used as a template to pick more particles in CTF-corrected tomograms with PyTOM template matching on all tomograms[38], as for the inner coat. Particles were cleaned based on their proximity to the membrane of the vesicles. Particles were aligned in Dynamo again, and the resulting Dynamo table was converted to a .star file using *dynamo2relion*.

Vertex particles were imported into RELION 5.0 and extracted as pseudo-subtomograms in a box size of 64 voxels and at a pixel size of 6.104 Å/px (bin4). Particles were cleaned using 3D classification with refinement restricting the Tilt and Psi Euler angles (*--sigma_rot 4 --sigma_psi 4*) but leaving in-plane rotation free. 3D classification used 3 classes, a T value of 0.25, and a particle diameter of 600 Å. Particles containing the vertex were then refined under the same conditions used in 3D classification. Particles were extracted at bin2 and further refined. Tomo frame alignment, Tomo Ctf refinement, and subsequent refinement at bin2 was iteratively repeated until resolution improvements stopped.

Outer coat (rod): Outer coat rods were manually picked in all tomograms, as before for the inner coat particles. Particles were assigned Euler angles normal to their nearest membrane. Particles were extracted, averaged to form a reference, and aligned in Dynamo, as per the outer coat vertices. Rods of different length were selected and isolated using Neighbour Analysis. The resulting Dynamo table was converted to a .star file using *dynamo2relion*.

Rod particles were imported into RELION 5.0 and extracted as pseudo-subtomograms in a box size of 64 voxels at a pixel size of 12.208 Å/px (bin8). As for the outer coat vertices, particles were progressively unbinned from bin8 to bin2 and refined with restrictions to apply local Euler angle searches.

GUVs-Sed5 Dataset

Inner coat: The surface of tubes in RELION-reconstructed tomograms was defined and segmented using the Pick Particle plug-in in Chimera as described previously[41,42]. The surface of the tube was oversampled, and coordinates were assigned Euler angles normal to the membrane. Particles were extracted in 32 voxel boxes from RELION-reconstructed tomograms at a voxel size of 10.8 Å. Particles were then aligned and averaged in Dynamo as before for the microsome inner coat dataset with several exceptions: in-plane rotation was restricted to 20 ° with azimuth flipping enabled; C1 symmetry was applied; particle translation was limited 15 voxels in all directions; alignment was carried out for 1 iteration. Duplicates defined as particles within 4 voxels of another particle, were deleted with Dynamo's separation in tomogram function during alignment. A previous inner coat structure (EMD-11199)[16] was low-pass filtered and used as a reference. Particles were cleaned by Neighbour Analysis as before for the microsome inner coat dataset. The resulting Dynamo table was converted to a .star file using *dynamo2relion*.

Particles were imported into RELION 5.0 and extracted as pseudo-subtomograms at bin8. They were refined and progressively unbinned iteratively until bin1 before Tomo Frame Refinement and Tomo Ctf Refinement as previously described[16]. The map was sharped using RELION's LocalRes sharpening with a -50 B-factor.

Outer coat (vertex): To pick outer coat vertices, we used the refined coordinates for the inner coat lattice and radially shifted them away from the membrane by 12 pixels. We then extracted these particles in a 64 voxel box size from RELION-reconstructed tomograms using Dynamo before aligning to a low pass filtered of a previous vertex structure (EMDB-11194)[15]. Alignment parameters were the same as was used for the inner coat alignment from the GUVs-Sed5 dataset except C2 symmetry was applied. The resulting Dynamo table was converted to a .star file using *dynamo2relion*.

Vertex particles were imported into RELION 5.0 and extracted as pseudo-subtomograms in a box size of 128 voxels at bin4. As for the outer coat vertices from microsomes, particles were progressively unbinned from bin8 to bin2 and refined with restrictions to apply local Euler angle searches. The map was sharped using RELION's LocalRes sharpening with a -175 B-factor.

Outer coat (rod): To pick outer coat rods, we used the refined coordinates of the outer coat vertices and used Dynamo's subboxing function to create 4 new coordinates where the rods

are placed relative to each vertex. As before for the outer coat vertices, particles were aligned in Dynamo to a low pass filtered reference (EMDB-11193)[15]. Particles were cleaned by Neighbour Analysis and duplicates were deleted. The resulting Dynamo table was converted to a .star file using *dynamo2relion*.

Rod particles were imported into RELION 5.0 and extracted as pseudo-subtomograms in a box size of 128 voxels at bin4. As for the outer coat rods from microsomes, particles were progressively unbinned from bin8 to bin2 and refined with restrictions to apply local Euler angle searches.

In all cases, relevant atomic model coordinates were rigid-body fitted into our maps using UCSF Chimera or ChimeraX. In all cases, fitting was unambiguous.

Acknowledgements

We thank Liz Miller at the MRC-LMB Cambridge for providing the microsomes, Natasha Lukoyanova and Shu Chen at the ISMB Birkbeck Cryo-EM Lab, Zhengyi Yang and Wim Hagen at the EMBL Imaging Centre in Heidelberg, and eBIC for cryo-tomography data collection, David Houldershaw at Birkbeck College for computational support, and Katie Downes at the Crick for help with the figures. We thank Sander van der Verren at the Crick, Katie Downes and Liz Miller for comments on the paper.

We acknowledge the access and services provided by the Imaging Centre at the European Molecular Biology Laboratory (EMBL IC), generously supported by the Boehringer Ingelheim Foundation. We acknowledge the ISMB EM facility (Birkbeck College, University of London), supported by the Wellcome Trust (202679/Z/16/Z and 206166/Z/17/Z). This work was supported by grants from: the European Research Council (ERC-StG-2019 grant 852915) and the BBSRC (BBSRC grant BB/T002670/1) to G.Z.

Additional Information

Competing Interests

The authors declare that no competing interests exist.

Author Contributions

Conceptualisation: G.Z.; Funding acquisition: G.Z.; Sample preparation: E.P.; Cryo-electron tomography data collection: E.P..; Cryo-electron tomography and STA data processing: E.P., G.Z.; Writing: (original draft) E.P., G.Z., (revisions) E.P., G.Z.

Data Availability

Data supporting the findings of this paper are available from the corresponding author upon reasonable request.

We have deposited the EM maps and models to the Electron Microscopy Data Bank with accession codes:

COPII Inner Coat on Vesicles: EMDB-19417

COPII Outer Coat (Rod) on Vesicles: EMD-19421

COPII Outer Coat (Vertex) on Vesicles: EMD-19418

COPII Inner Coat on Tubes with Sed5: EMDB-19410

COPII Outer Coat (Rod) on Tubes with Sed5: EMDB-19414

COPII Outer Coat (Vertex) on Tubes with Sed5: EMDB-19416

References

1. Jamieson, J. D. & Palade, G. E. INTRACELLULAR TRANSPORT OF SECRETORY PROTEINS IN THE PANCREATIC EXOCRINE CELL : III. Dissociation of Intracellular Transport from Protein Synthesis. *Journal of Cell Biology* **39**, 580–588 (1968).
2. Novick, P., Ferro, S. & Schekman, R. Order of events in the yeast secretory pathway. *Cell* **25**, 461–469 (1981).
3. Zanetti, G., Pahuja, K. B., Studer, S., Shim, S. & Schekman, R. COPII and the regulation of protein sorting in mammals. *Nature Cell Biology* **14**, 20–28 (2012).
4. Lee, M. C. S. *et al.* Sar1p N-terminal helix initiates membrane curvature and completes the fission of a COPII vesicle. *Cell* **122**, 605–617 (2005).
5. Barlowe, C. & Schekman, R. SEC12 encodes a guanine-nucleotide-exchange factor essential for transport vesicle budding from the ER. *Nature* **365**, 347–349 (1993).
6. Miller, E., Antonny, B., Hamamoto, S. & Schekman, R. Cargo selection into COPII vesicles is driven by the Sec24p subunit. *The EMBO Journal* **21**, 6105–6113 (2002).
7. Novick, P., Field, C. & Schekman, R. Identification of 23 complementation groups required for post-translational events in the yeast secretory pathway. *Cell* **21**, 205–215 (1980).

8. Bi, X., Mancias, J. D. & Goldberg, J. Insights into COPII coat nucleation from the structure of Sec23.Sar1 complexed with the active fragment of Sec31. *Dev. Cell* **13**, 635–645 (2007).
9. Fath, S., Mancias, J. D., Bi, X. & Goldberg, J. Structure and organization of coat proteins in the COPII cage. *Cell* **129**, 1325–1336 (2007).
10. Stagg, S. M. *et al.* Structure of the Sec13/31 COPII coat cage. *Nature* **439**, 234–238 (2006).
11. Stagg, S. M. *et al.* Structural basis for cargo regulation of COPII coat assembly. *Cell* **134**, 474–484 (2008).
12. Antonny, B., Madden, D., Hamamoto, S., Orci, L. & Schekman, R. Dynamics of the COPII coat with GTP and stable analogues. *Nature Cell Biology* **3**, 531–537 (2001).
13. Zanetti, G. *et al.* The structure of the COPII transport-vesicle coat assembled on membranes. *Elife* **2**, e00951 (2013).
14. Hutchings, J., Stancheva, V., Miller, E. A. & Zanetti, G. Subtomogram averaging of COPII assemblies reveals how coat organization dictates membrane shape. *Nature Communications* **9**, 4154 (2018).
15. Hutchings, J. *et al.* Structure of the complete, membrane-assembled COPII coat reveals a complex interaction network. *Nature Communications* **12**, 2034 (2021).
16. Zivanov, J. *et al.* A Bayesian approach to single-particle electron cryo-tomography in RELION-4.0. *Elife* **11**, e83724 (2022).
17. Čopič, A., Latham, C. F., Horlbeck, M. A., D'Arcangelo, J. G. & Miller, E. A. ER Cargo Properties Specify a Requirement for COPII Coat Rigidity Mediated by Sec13p. *Science* **335**, 1359–1362 (2012).
18. Ma, W. & Goldberg, J. TANGO1/cTAGE5 receptor as a polyvalent template for assembly of large COPII coats. *PNAS* **113**, 10061–10066 (2016).
19. Saito, K., Maeda, M. & Katada, T. Regulation of the Sar1 GTPase Cycle Is Necessary for Large Cargo Secretion from the Endoplasmic Reticulum. *Front Cell Dev Biol* **5**, 75 (2017).
20. Staehelin, L. A. & Kang, B.-H. Nanoscale Architecture of Endoplasmic Reticulum Export Sites and of Golgi Membranes as Determined by Electron Tomography. *Plant Physiol* **147**, 1454–1468 (2008).
21. Bykov, Y. S. *et al.* The structure of the COPI coat determined within the cell. *eLife* https://elifesciences.org/articles/32493 (2017) doi:10.7554/eLife.32493.
22. Melero, A., Boulanger, J., Kukulski, W. & Miller, E. A. Ultrastructure of COPII vesicle formation in yeast characterized by correlative light and electron microscopy. *Mol Biol Cell* **33**, ar122 (2022).
23. Castaño-Díez, D. & Zanetti, G. In situ structure determination by subtomogram averaging. *Curr. Opin. Struct. Biol.* **58**, 68–75 (2019).

24. Pyle, E. & Zanetti, G. Current data processing strategies for cryo-electron tomography and subtomogram averaging. *Biochem J* **478**, 1827–1845 (2021).
25. Mossessova, E., Bickford, L. C. & Goldberg, J. SNARE selectivity of the COPII coat. *Cell* **114**, 483–495 (2003).
26. Miller, E. A. *et al.* Multiple cargo binding sites on the COPII subunit Sec24p ensure capture of diverse membrane proteins into transport vesicles. *Cell* **114**, 497–509 (2003).
27. Bacia, K. *et al.* Multibudded tubules formed by COPII on artificial liposomes. *Sci Rep* **1**, 17 (2011).
28. Stancheva, V. G. *et al.* Combinatorial multivalent interactions drive cooperative assembly of the COPII coat. *J Cell Biol* **219**, (2020).
29. Angelova, M. I. & Dimitrov, D. S. Liposome electroformation. *Faraday Discuss. Chem. Soc.* **81**, 303–311 (1986).
30. Matsuoka, K. *et al.* COPII-coated vesicle formation reconstituted with purified coat proteins and chemically defined liposomes. *Cell* **93**, 263–275 (1998).
31. Hagen, W. J. H., Wan, W. & Briggs, J. A. G. Implementation of a cryo-electron tomography tilt-scheme optimized for high resolution subtomogram averaging. *J. Struct. Biol.* **197**, 191–198 (2017).
32. Mastronarde, D. N. Automated electron microscope tomography using robust prediction of specimen movements. *J. Struct. Biol.* **152**, 36–51 (2005).
33. Eisenstein, F. *et al.* Parallel cryo electron tomography on in situ lamellae. *Nat Methods* **20**, 131–138 (2023).
34. Zheng, S. Q. *et al.* MotionCor2: anisotropic correction of beam-induced motion for improved cryo-electron microscopy. *Nat. Methods* **14**, 331–332 (2017).
35. Zivanov, J., Nakane, T. & Scheres, S. H. W. A Bayesian approach to beam-induced motion correction in cryo-EM single-particle analysis. *IUCrJ* **6**, 5–17 (2019).
36. Rohou, A. & Grigorieff, N. CTFFIND4: Fast and accurate defocus estimation from electron micrographs. *J. Struct. Biol.* **192**, 216–221 (2015).
37. Liu, Y.-T. *et al.* Isotropic reconstruction for electron tomography with deep learning. *Nat Commun* **13**, 6482 (2022).
38. Chaillet, M. L. *et al.* Extensive Angular Sampling Enables the Sensitive Localization of Macromolecules in Electron Tomograms. *Int J Mol Sci* **24**, 13375 (2023).
39. Mastronarde, D. N. & Held, S. R. Automated tilt series alignment and tomographic reconstruction in IMOD. *J. Struct. Biol.* **197**, 102–113 (2017).
40. Castaño-Díez, D., Kudryashev, M., Arheit, M. & Stahlberg, H. Dynamo: a flexible, user-friendly development tool for subtomogram averaging of cryo-EM data in high-performance computing environments. *J. Struct. Biol.* **178**, 139–151 (2012).

41. Pyle, E., Hutchings, J. & Zanetti, G. Strategies for Picking Membrane-Associated Particles within Subtomogram Averaging Workflows. *Faraday Discuss.* (2022) doi:10.1039/D2FD00022A.

42. Qu, K. *et al.* Maturation of the matrix and viral membrane of HIV-1. *Science* **373**, 700–704 (2021).

43. Pettersen, E. F. *et al.* UCSF Chimera--a visualization system for exploratory research and analysis. *J Comput Chem* **25**, 1605–1612 (2004).

Supplementary Figures

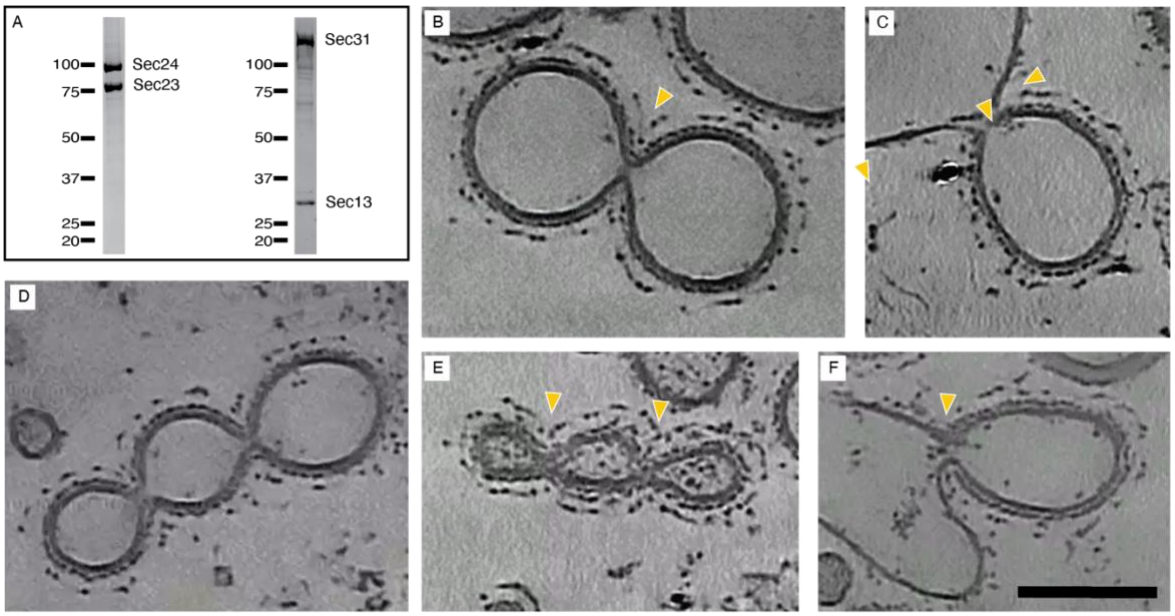

Supplementary Figure 1: (A) Polyacrylamide gel of purified Sec23-Sec24 and Sec13-Sec31 complexes from insect cell expression. (B-F) XY slices through reconstructed tomograms that show rare events with constricted but not detached vesicle necks (yellow arrowheads).

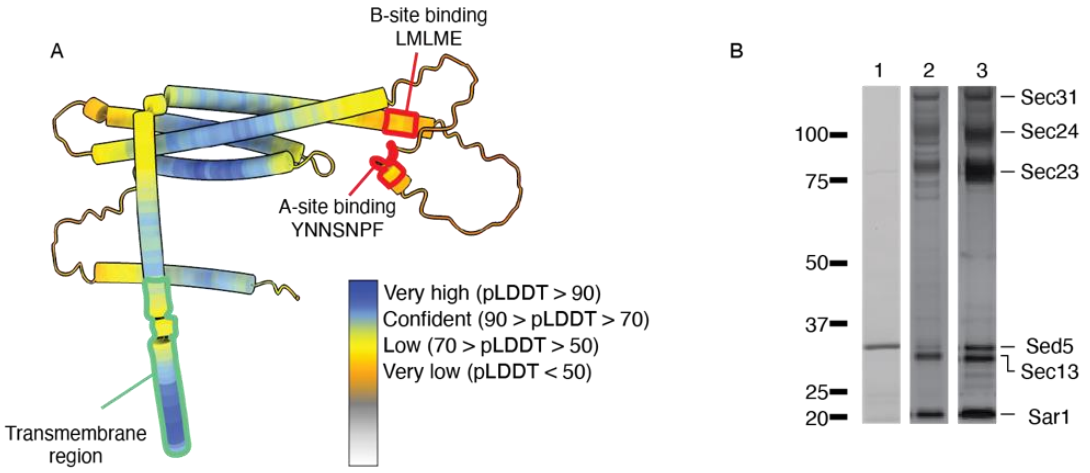

Supplementary Figure 2: (A) Alpha-fold prediction of the full-length Sed5 structure (PDB ID: AF-Q01590-F1), coloured according to pLDDT value. The C-terminal transmembrane domain is highlighted in green, whilst the two Sec24-binding peptides are highlighted in red. These both fall within very low confidence regions, indicating disorder/flexibility. (B) Acrylamide gel showing purified Sed5 (lane 1), pelleted (lane 2) and floating (lane 3) fractions from a liposome flotation experiment.

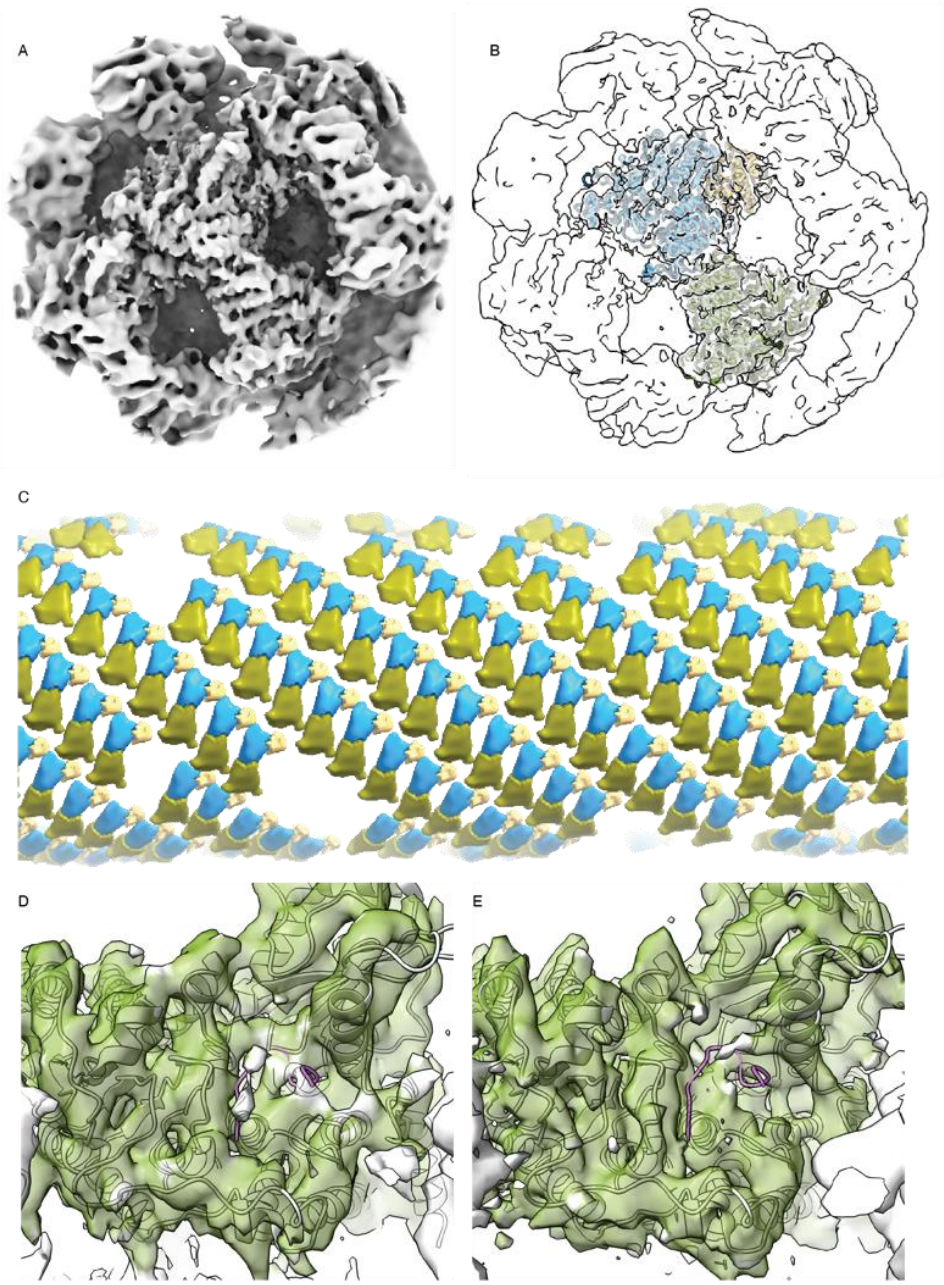

Supplementary Figure 3: (A) Surface representation of the 4.1 Å STA map of the inner coat on Sed5-enriched GUV tubules (B) as in (A), with the Sec24-Sec24-Sar1 heterotrimer atomic model fitted. Sec23 in blue, Sec24 in green, Sar1 in yellow. (C) A 20 Å low-pass filtered map of the inner coat mapped back onto a representative section of a tomogram, showing the extensive lattice wrapping around a tubule. (D) and (E), As in Figure 3E and 3F, but focussing on the A-site of Sec24, and showing the Sed5 YNNSNPF peptide bound as crystallised (PDB ID: 8PD0, in purple). While extra density in (D) (Sed5-bound) with respect to (E) cannot be excluded, it is difficult to unambiguously detect above the noise.

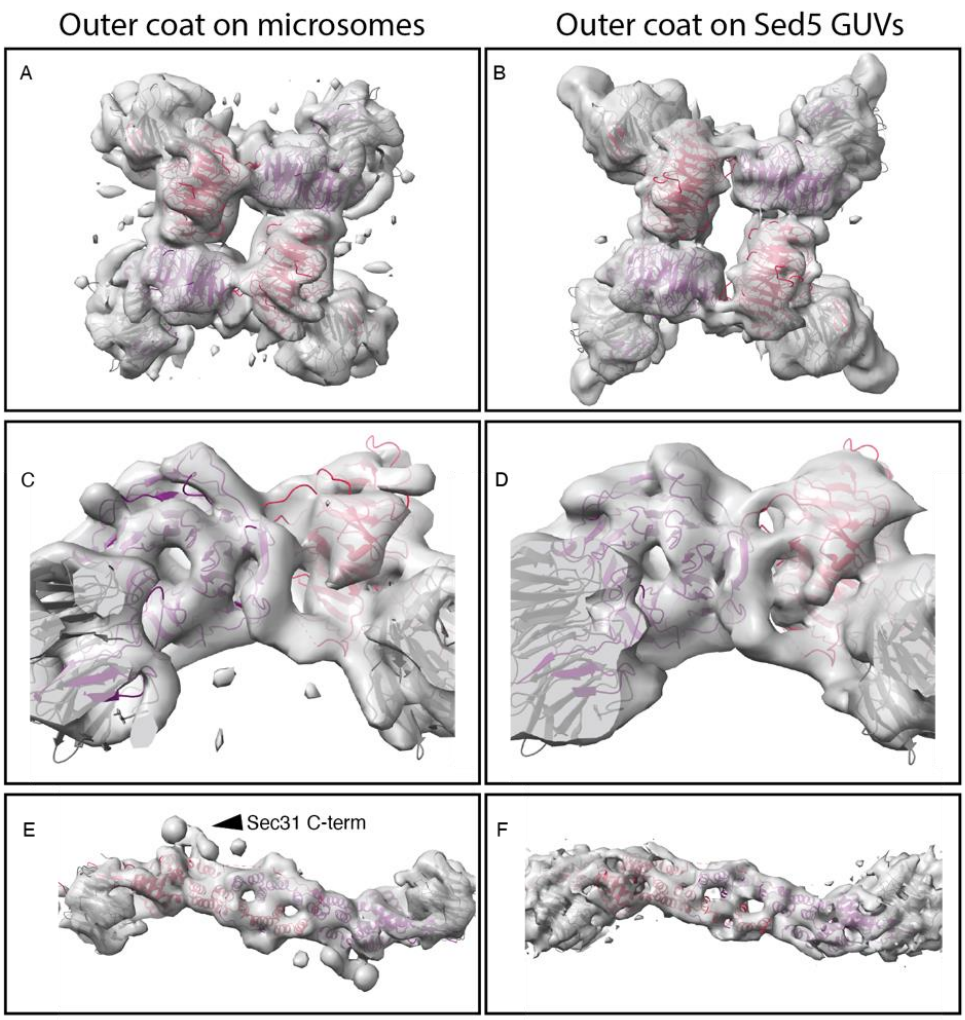

Supplementary Figure 4: Comparison between the outer coat STA maps obtained from microsome and Sed5-GUV derived vesicles and tubes respectively. (A,B) overview of vertices, with four copies of the atomic model of the Sec13-Sec31 'vertex element' fitted (PDB 2PM9). Sec31 in red and purple, Sec13 in grey. (C,D) close up of the vertices from a side view. (E,F), overview of rods, with the atomic model of the Sec13-Sec31 'edge' element fitted (PDB 2PM6). Colour code as in (A,B).